mater.scichina.com link.springer.com

Sci China Mater 2025, 68(5): 1408–1414
https://doi.org/10.1007/s40843-024-3277-8

SPECIAL TOPIC: Photovoltaic Materials, Devices, and Applications

Central fluorination strategy of biphosphonic acid molecule for self-assembled monolayer enables efficient organic solar cells

Hang Liu[1†], Xingbang Gao[1†], Yufei Xin[1], Ruohan Wang[1], Haolin Zhong[1], Bin Kan[3], Xiangjian Wan[1,2], Yongsheng Chen[1,2] and Yongsheng Liu[1,2*]

ABSTRACT **Poly(3,4-ethylenedioxythiophene):poly(4-styrenesulfonate) (PEDOT:PSS) is a primary hole extraction layer (HEL) employed in most state-of-the-art regular organic solar cells (OSCs). However, the acidic nature of PEDOT:PSS could corrode the indium tin oxide (ITO) electrode under prolonged operation, compromising the long-term stability of the devices. Herein, we have designed and synthesized a novel biphosphonic acid molecule, namely 3BPIC-*c*F, for self-assembled monolayers (SAMs) using a central fluorination strategy. Compared to PEDOT:PSS, the 3BPIC-*c*F-modified ITO substrate exhibits enhanced light transmittance and improved interfacial compatibility with the organic active layer. Thanks to the introduction of fluorine atoms, 3BPIC-*c*F exhibits a larger dipole moment and a deeper highest occupied molecular orbital energy level, leading to an increased work function for the ITO/3BPIC-*c*F substrate compared to the ITO/PEDOT:PSS substrate. These advantages can enhance hole extraction within the device, decrease interfacial impedance and restrain nonradiative recombination at the interface. Consequently, OSCs utilizing 3BPIC-*c*F as HEL achieved a high efficiency of 19.34%, surpassing the performance of devices based on PEDOT:PSS (power conversion efficiency (PCE) = 18.64%). Importantly, the OSCs based on 3BPIC-*c*F exhibit significantly improved stability compared to those using PEDOT:PSS. This research provides valuable insights for the development of functional molecules for SAMs, with the potential to enhance the performance of organic solar cells.**

Keywords: organic solar cells, self-assembled monolayer, fluorination strategy, hole extraction layer

INTRODUCTION

As a promising next-generation photovoltaic technology, organic solar cells (OSCs) have attracted considerable attention due to their advantages such as lightweight, mechanical flexibility and low cost [1–9]. Recently, the power conversion efficiency (PCE) of single junction OSCs has exceeded 20% benefiting from the rapid development of near-infrared (NIR) non-fullerene acceptors (NFAs) and polymer donors [10–22]. Additionally, as an important component of OSCs, the charge transport layers (CTLs) also play a crucial role in carrier transport and the suppression of non-radiative recombination at the interface [23–25]. So far, most regular OSCs mainly employed poly(3,4-ethylenedioxythiophene):poly(4-styrenesulfonate) (PEDOT:PSS) as hole extraction layer (HEL) [5,23,26]. However, the acidic nature of the PSS component can corrode the indium tin oxide (ITO) electrode over time, potentially compromising the long-term stability of the devices [27,28]. Therefore, it is critical to develop new alternatives to replace PEDOT:PSS in order to improve the long-term stability and efficiency of OSCs.

Self-assembled monolayers (SAMs) have gained considerable attention in perovskite solar cells due to their advantageous properties, including a simple molecular structure, low synthesis cost, low material usage, and tunable energy levels [29–35]. In recent years, SAMs have also been progressively explored as HEL in OSCs and achieved rapid progress. However, most of the SAMs used in OSCs are monophosphonic (2-(9*H*-carbazol-9-yl)ethyl)phosphonic acid (2PACz) and its derivates [28,36–39]. The increase in the number of phosphonic acid anchoring groups could enhance their adsorption onto the surface of ITO and improve the molecular coverage of SAM [40]. Nevertheless, SAMs based on multiple phosphonic acid moleculars have been seldom reported in the field of OSCs [30,31,41].

Previous works have revealed that for hole-extractive SAM molecules, the increase of molecular dipole moment can enlarge the work function (WF) of ITO/SAM substrate, thus promoting more efficient hole extraction from the active layer [30,31,41]. In this work, we successfully designed and synthesized a novel SAM molecule, 3BPIC-*c*F, based on fluorine modified indolo[2,3-*a*]-carbazole conjugate cores utilizing a central fluorination strategy (Fig. 1a). Thanks to the fluorine modification in the indolo[2,3-*a*]carbazole core, 3BPIC-*c*F exhibits an enlarged dipole moment in comparison with 3BPIC, resulting in an increased WF for the ITO/3BPIC-*c*F substrate, thereby facilitating efficient hole extraction. Compared to PEDOT:PSS, 3BPIC-*c*F modified ITO exhibits a higher light transmittance due to the ultra-thin

[1] The Centre of Nanoscale Science and Technology and Key Laboratory of Functional Polymer Materials, Institute of Polymer Chemistry, College of Chemistry, Nankai University, Tianjin 300071, China
[2] Renewable Energy Conversion and Storage Center, Nankai University, Tianjin 300071, China
[3] School of Materials Science and Engineering, National Institute for Advanced Materials, Nankai University, Tianjin 300350, China
[†] Equally contributed to this work.
[*] Corresponding author (email: liuys@nankai.edu.cn)

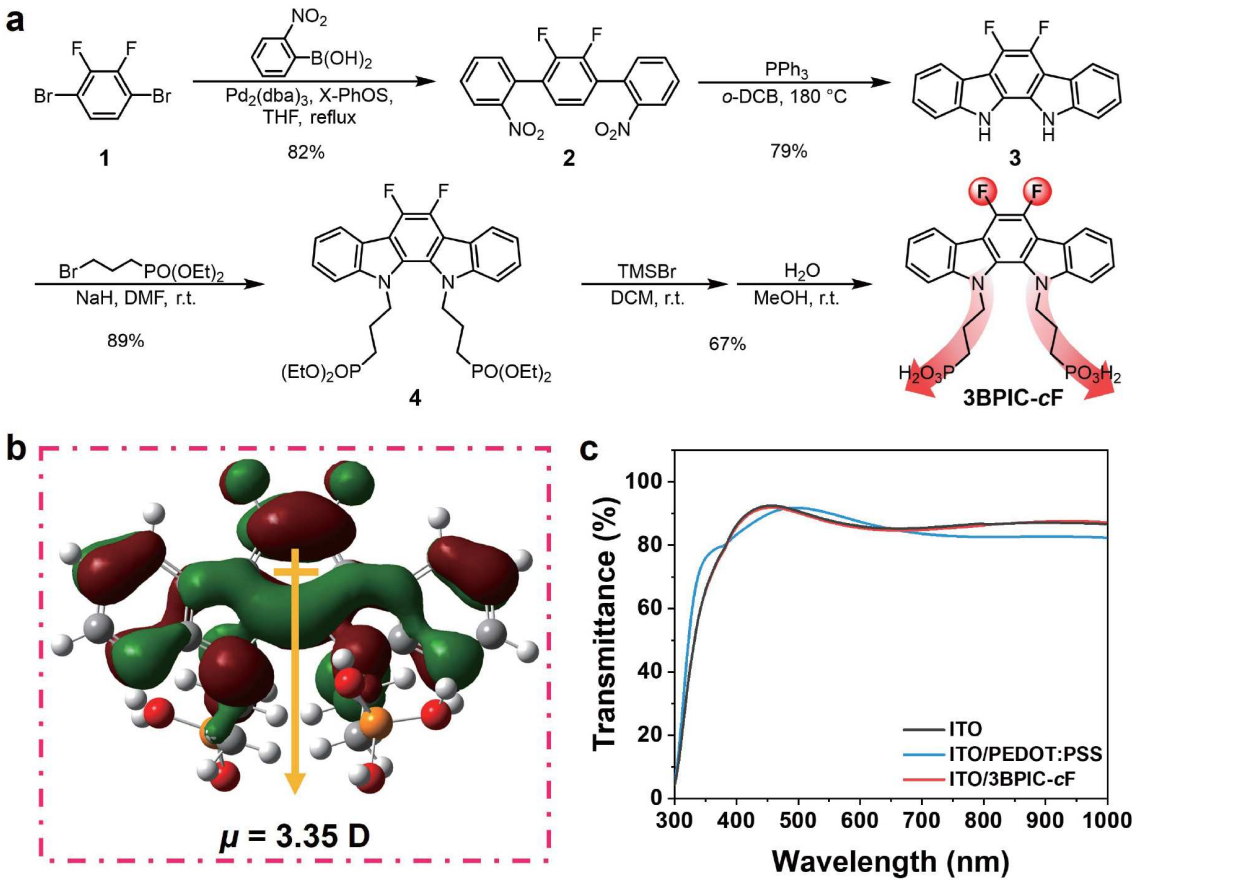

Figure 1 (a) Synthetic route of 3BPIC-*c*F SAM; (b) calculated HOMO orbital distributions, dipole moments and HOMO energy levels of 3BPIC-*c*F SAMs. (c) ultraviolet-visible transmittance spectra of ITO with various HELs.

monolayer with minimal light absorption, leading to improved light utilization. Moreover, the fused aromatic structure on the opposite side of the phosphonic acid groups enhances their interfacial compatibilities with the photoactive layer. As a result, the 3BPIC-*c*F-based device achieved a champion PCE of 19.34%, much higher than the PEDOT:PSS-based device (PCE = 18.64%). Moreover, the device based on 3BPIC-*c*F displayed superior thermal stability compared to the PEDOT:PSS-based device.

RESULTS AND DISCUSSION

To improve the dipole moment of biphosphonic acid molecules in the SAM layer, we designed and synthesized a conjugated core-based SAM molecule, 3BPIC-*c*F, incorporating an indolo[2,3-*a*]carbazole structure and employing a central fluorination strategy. The synthetic route for 3BPIC-*c*F is shown in Fig. 1a, with the detailed synthesis process provided in the Supplementary information. We first prepared the intermediate, 2′,3′-difluoro-2,2″-dinitro-1,1′:4′,1″-terphenyl (Compound 2), through a $Pd_2(dba)_3$ catalyzed Suzuki cross-coupling reaction of (2-nitrophenyl)boronic acid and 1,4-dibromo-2,3-difluorobenzene (Compound 1). The ligand 2-dicyclohexylphosphino-2′,4′,6′-tri-i-propyl-1,1′-biphenyl (X-PHOS) was used to overcome the influence of steric hindrance. From this intermediate, the central fluorinated indolo[2,3-*a*]carbazole core was successfully synthesized with a yield of 79% utilizing the Cadogan reaction. Under optimized reaction conditions, the target molecule 3BPIC-*c*F was synthesized successfully through an SN_2 substitution reaction and a hydrolysis reaction. The SAM 3BPIC-*c*F was further characterized by nuclear magnetic resonance (NMR) and high-resolution mass spectrometry (HRMS) (Figs S25–S29). The ^{13}C NMR spectra (Fig. S26) show three doublet-of-doublets (dd) peaks at chemical shifts of 139.02, 125.08 and 112.35 ppm, indicating the varying degrees of coupling splitting of the two F atoms with the three different C atoms of the central benzene ring. The coupling constants decrease as the distances between C and F increase.

The highest occupied molecular orbital (HOMO) and lowest unoccupied molecular orbital (LUMO) distributions from density functional theory (DFT) calculation (B3LYP/6-31G(d)) show that 3BPIC-*c*F exhibits a deeper HOMO energy level of −5.33 eV than that of PEDOT (−4.43 eV) (Fig. S1). More importantly, the higher dipole moment of 3BPIC-*c*F (μ = 3.35 D) contributes to the low-lying WF of ITO/3BPIC-*c*F substrate discussed below. The ITO/3BPIC-*c*F substrate exhibits similar light transmittance to that of bare ITO (Fig. 1c), resulting in much enhanced light utilization compared to the ITO/PEDOT:PSS anode. According to ultraviolet photoelectron spectrometry (UPS) analysis (Fig. 2a), the HOMO energy levels of the ITO/3BPIC-*c*F and ITO/PEDOT:PSS substrates are −5.49 and −5.38 eV (Fig. 2b), respectively, showing the same trend as observed from DFT calculations. Moreover, the WF of ITO/3BPIC-*c*F is 5.14 eV, showing a sequential increase from 4.70 eV for bare ITO to 4.75 eV for ITO/PEDOT:PSS (Fig. 2b). The

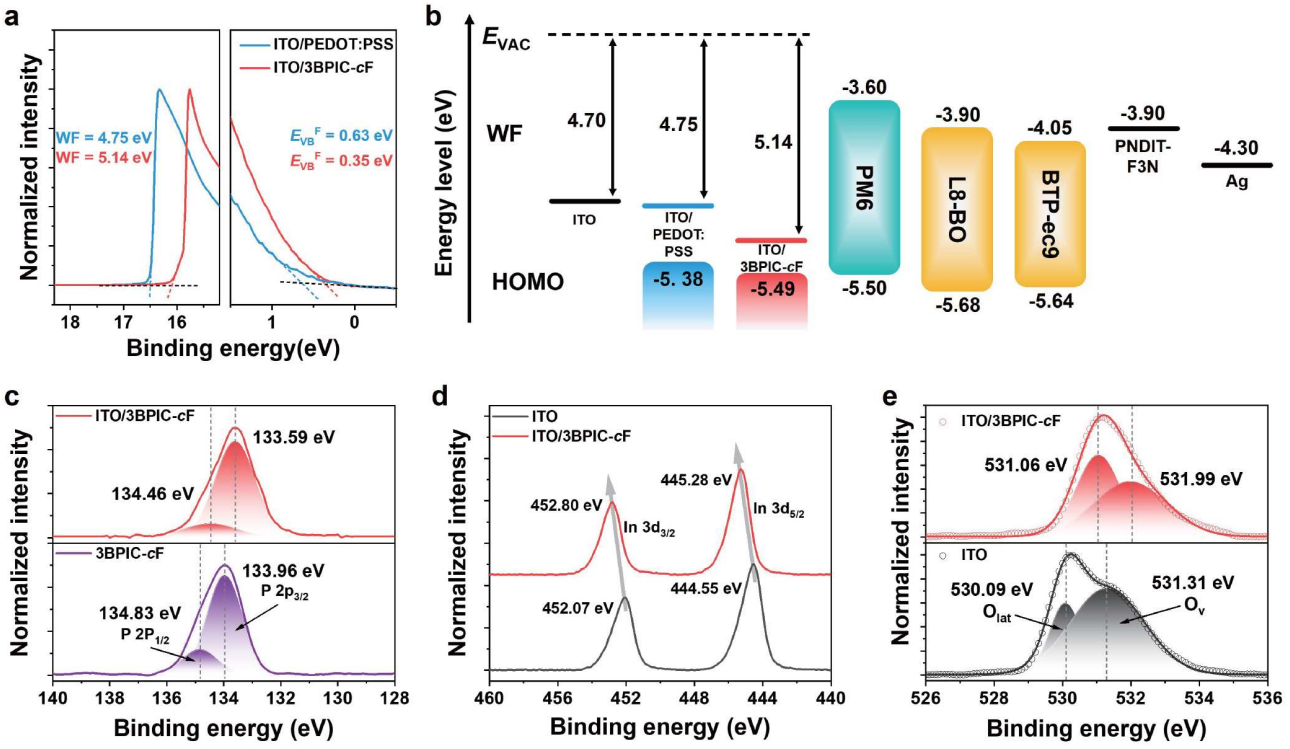

Figure 2 (a) UPS spectra of ITO/3BPIC-*c*F and ITO/PEDOT:PSS; (b) schematic diagram of energy level arrangement; (c) P 2p, (d) In 3d and (e) O 1s core level XPS spectra of bare ITO and ITO/3BPIC-*c*F films.

enlarged WF of ITO/3BPIC-*c*F can be attributed to the larger dipole moment of 3BPIC-*c*F, as calculated from DFT calculation (Fig. 1b), thereby enhancing its compatibility with the HOMO energy level of the polymer donor PM6 (chemical structure shown in Fig. S5) in the photoactive layer [42,43]. The larger WF and deeper HOMO level of ITO/3BPIC-*c*F will facilitate hole extraction at the interface by reducing energy loss to achieve a higher open-circuit voltage (V_{OC}) of the corresponding OSCs [42,44].

The interactions between the 3BPIC-*c*F molecule and the ITO surface were investigated using X-ray photoelectron spectroscopy (XPS). As shown in Fig. 2c and Table S1, the P $2p_{1/2}$ and P $2p_{3/2}$ peaks of pure 3BPIC-*c*F were located at 134.83 and 133.96 eV, respectively. After being coated on the ITO surface, these peaks shifted to 134.46 and 133.59 eV, respectively. Similarly, the In $3d_{3/2}$ and In $3d_{5/2}$ peaks for bare ITO were observed at 452.07 and 444.55 eV, respectively, while for 3BPIC-*c*F-covered ITO, they shifted to 452.80 and 445.28 eV, respectively. A comparable trend was observed for the Sn 3d peaks (Fig. S2 and Table S1). Regarding the lattice oxygen (O_{lat}) on the ITO surface, the O 1s peaks for bare ITO and ITO/3BPIC-*c*F were located at 530.09 and 531.06 eV, respectively (Fig. 3e). The obvious shifts of the P 2p, In 3d, Sn 3d and O 1s orbitals indicate that 3BPIC-*c*F has chemically adsorbed onto the ITO surface [31,45]. In addition, the ratio of vacancy oxygen (O_v) to O_{lat} decreased from 2.83 for ITO to 1.11 for ITO/3BPIC-*c*F (Fig. 3e, Fig. S3 and Table S1), suggesting that oxygen vacancy defects were effectively passivated by phosphonic acid groups. This passivation could help reduce trap-assisted nonradiative recombination in OSCs [45].

The contact angle (CA) measurements were performed using water and diiodomethane (DIM) to evaluate the interface compatibility between the substrate and the active layer. As shown in Fig. S4, the water contact angle of ITO/PEDOT:PSS was measured to be 15.62°, significantly smaller than that of ITO/3BPIC-*c*F, which was 76.17°. The DIM contact angle shows that the ITO/PEDOT:PSS substrate has a larger value of 42.77° compared to 34.87° for ITO/3BPIC-*c*F. These results indicate that 3BPIC-*c*F SAMs enhance the interface contact between the organic active layer and the substrate, which facilitates carrier transport.

To compare the photovoltaic performance of 3BPIC-*c*F and PEDOT:PSS as HELs in OSCs, we fabricated the devices using a conventional structure of ITO/HEL/bulk heterojunction (BHJ)/PNDIT-F3N/Ag (Fig. 3a), with PM6:L8-BO:BTP-ec9 (chemical structure shown in Fig. S5) as the BHJ layer [20]. The preparation process of SAM-modified ITO followed a previous method in our group [41]. The current density–voltage (*J*–*V*) curves of the OSCs in Fig. 3b show that the device based on PEDOT:PSS exhibits a V_{OC} of 0.881 V, a short-circuit current density (J_{SC}) of 27.15 mA cm^{-2}, and a fill factor (FF) of 77.90%, achieving a PCE of 18.64% (Table 1). In comparison, the optimized OSCs using biphosphonic acid 3BPIC-*c*F SAM as the HEL showed an enlarged V_{OC} of 0.889 V, a notable J_{SC} of 27.98 mA cm^{-2} and an FF of 77.73%, yielding a champion PCE of 19.34%, which is much higher than that of the PEDOT:PSS-based device (Table 1). The distributions of photovoltaic parameters for OSCs with different HELs are shown in Fig. 3c and Fig. S6. The statistical analysis of PCEs indicates that the devices based on 3BPIC-*c*F have an average PCE of 19.04%, surpassing the PEDOT:PSS devices, which have an average PCE of 18.32%. Moreover, the 3BPIC-*c*F-based device demonstrates superior performance compared to the device using conventional 2PACz as the HEL (PCE = 18.99%) (Figs S7, S8 and Table S2). This

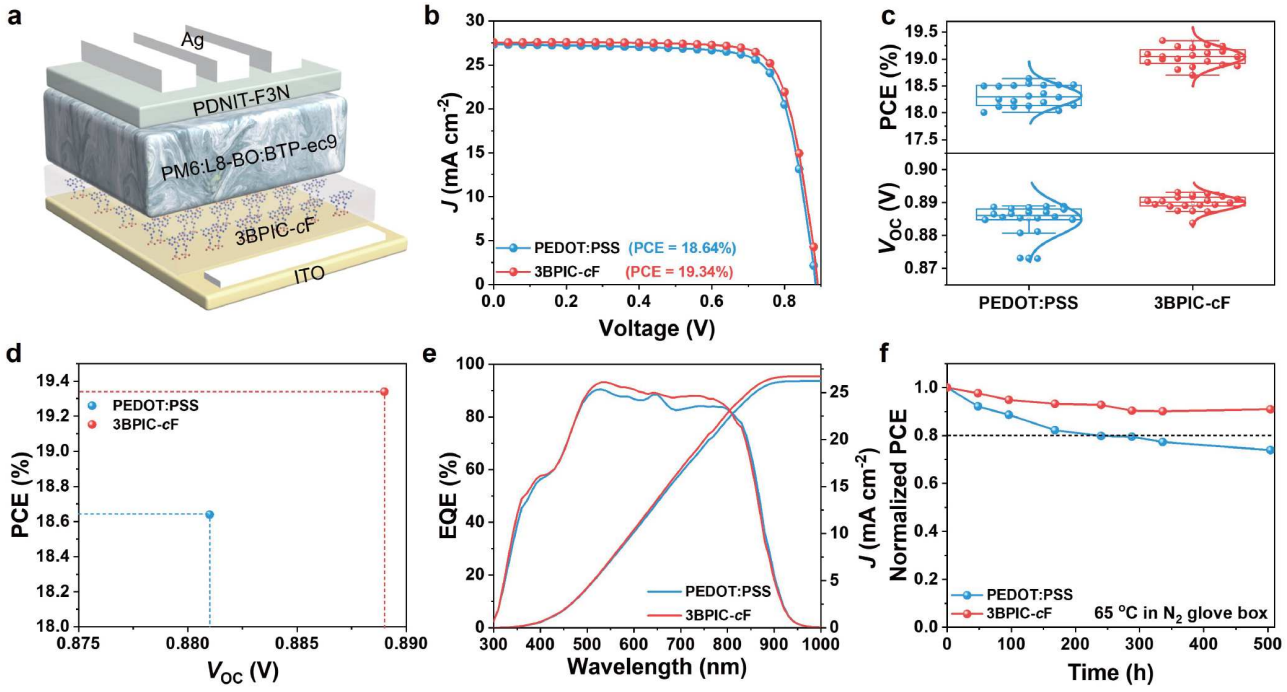

Figure 3 (a) Device architecture of the conventional OSCs based on 3BPIC-*c*F; (b) *J*–*V* characteristics curves of the optimized PM6:L8-BO:BTP-ec9 devices based on PEDOT:PSS and 3BPIC-*c*F; (c) statistical PCE and V_{OC} data of the corresponding devices; (d) the relationship of PCE and V_{OC} of the corresponding devices; (e) EQE spectra and integrated photocurrent density of the corresponding devices; (f) thermal aging test of unencapsulated devices based on PEDOT:PSS and 3BPIC-*c*F under 65 °C in N_2 glovebox.

Table 1 Optimized photovoltaic parameters for devices based on 3BPIC-*c*F and PEDOT:PSS

BHJ	HELs	V_{OC} (V)	J_{SC} (mA cm^{-2})	J_{SC}^{a} (mA cm^{-2})	FF (%)	PCE (%)
PM6:L8-BO:BTP-ec9	PEDOT:PSS	0.881 (0.884 ± 0.005)	27.15 (26.98 ± 0.39)	26.22	77.90 (76.76 ± 0.50)	18.64 (18.32 ± 0.20)
	3BPIC-*c*F	0.889 (0.890 ± 0.002)	27.98 (27.72 ± 0.19)	26.73	77.73 (77.30 ± 0.55)	19.34 (19.04 ± 0.17)

a) Calculated from EQE data.

improvement is attributed to the more uniform coverage of 3BPIC-*c*F on the ITO surface and the increased WF compared to 2PACz, as evidenced by the narrower and lower surface contact potential distribution observed in the Kelvin probe force microscopy (KPFM) results (Fig. S9). As shown in Fig. 3d, the improved PCE in the 3BPIC-*c*F-based devices is mainly attributed to an increase in V_{OC}, which could be linked to the enlarged WF of ITO/3BPIC-*c*F and the reduced built-in voltage (V_{bi}) of the device, as discussed below. Additionally, the integrated J_{SC} of the OSCs based on PEDOT:PSS and 3BPIC-*c*F, calculated from external quantum efficiency (EQE) curves (Fig. 3e), are 26.22 and 26.73 mA cm^{-2}, respectively, closely matching the *J*–*V* results with an error margin within 4%. This consistency was also confirmed in the *J*–*V* curves and EQE data of two additional high-efficiency device groups (Fig. S10 and Table S3). Beyond the improvement in PCEs, we also evaluated the stability of the unencapsulated OSCs. As shown in Fig. 3f and Fig. S11, the unencapsulated device based on 3BPIC-*c*F maintains over 90% of its initial PCE after aging for 500 h at 65 °C in a N_2 glove box, whereas the PCE of the device based on PEDOT:PSS decays to less than 80% of its initial value after 240 h. The operational stability was evaluated by tracking the PCE at the maximum power point (MPP) under continuous light illumination (white light-emitting diode (LED), 100 mW cm^{-2}). The 3BPIC-*c*F-based unencapsulated device maintained approximately 87% of its original PCE after 100 h (Fig. S12), surpassing the PEDOT:PSS-based device, which retained about 81% after the same period.

To study the carrier recombination kinetics in OSCs based on different HELs, light intensity-dependent *J*–*V* characteristics were evaluated. As shown in Fig. 4a, the Nyquist plot from the electrochemical impedance spectroscopy (EIS) measurements was obtained for OSCs with different SAMs. According to the equivalent circuit model, the series resistance (R_{series}) and charge-transport resistance (R_{ct}) for devices based on PEDOT:PSS are 18.4 and 71.9 Ω, respectively, while for those based on 3BPIC-*c*F, they are 16.5 and 66.1 Ω, respectively. The decrease in both R_{series} and R_{CT} in the 3BPIC-*c*F-based devices could be attributed to the ultra-thin monolayer and improved interface compatibility, which facilitate carrier transport and help suppress charge recombination [46]. The relationship between V_{OC} and light intensity (*I*) follows the formula $V_{OC} \propto nK_BT\ln(I)/q$, where K_B, *T*, *q*, and *n* are the Boltzmann constant, Kelvin temperature, elementary charge, and ideality factor, respectively [47]. The calculated *n* values for PEDOT:PSS and 3BPIC-*c*F-based OSCs are 1.342 and 1.214, respectively (Fig. 4b). Addi-

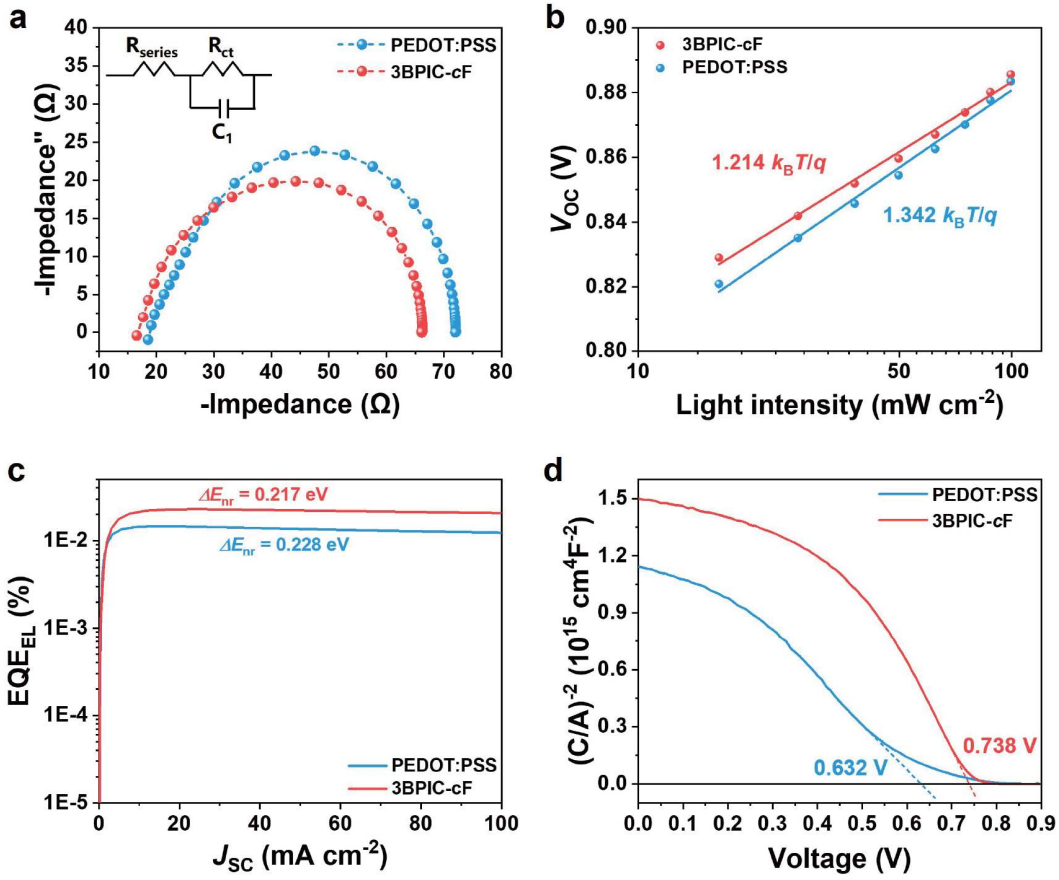

Figure 4 (a) Nyquist plots of the corresponding devices (inset: the equivalent-circuit model employed for fitting of EIS data); (b) V_{OC} versus light intensity for OSCs with different HELs; (c) the EQE_{EL} profiles of the corresponding devices; (d) Mott–Schottky plots of devices based on different HELs.

tionally, the J_{SC} versus light density curves show that the exponent α of PEDOT:PSS and 3BPIC-*c*F-based devices ($J_{SC} \propto I^{\alpha}$) is 0.989 and 0.993, respectively (Fig. S13). The lower n value and higher α value for the 3BPIC-*c*F-based devices suggest a reduction in trap-assisted recombination and bimolecular recombination [48,49].

The transient photovoltage (TPV) and transient photocurrent (TPC) measurements were carried out to study the carrier dynamic in the devices. As displayed in the TPV curves (Fig. S14a), the 3BPIC-*c*F-based device exhibits a significantly longer carrier lifetime of 58.0 μs than the PEDOT:PSS-based device (τ = 51.9 μs), suggesting suppressed nonradiative recombination in the 3BPIC-*c*F-based device. The TPC results in Fig. S14b show that the 3BPIC-*c*F-based device has a shorter decay time of 1.31 μs compared to 2.86 μs for the PEDOT:PSS-based device. The shorter decay time indicates faster charge collection in the 3BPIC-*c*F-based device.

To further evaluate the nonradiative recombination energy loss (ΔE_{nr}), the external electroluminescence yield (EQE_{EL}) was measured as a function of injection current by operating the OSC device as an LED. Using the equation $\Delta E_{nr} = -k_B T \ln(EQE_{EL})$ [50], the corresponding ΔE_{nr} values are 0.228 and 0.217 eV for PEDOT:PSS and 3BPIC-*c*F-based OSCs, respectively (Fig. 4c). The smaller ΔE_{nr} of the 3BPIC-*c*F-based device could be attributed to its higher WF and better interface compatibility as discussed above. Additionally, the Mott–Schottky analysis was performed to investigate the built-in voltage (V_{bi}) of OSCs based on different SAMs. As displayed in Fig. 4d, the OSC based on 3BPIC-*c*F exhibits a V_{bi} of 0.738 V, higher than that of the device based on PEDOT:PSS (V_{bi} = 0.632 V). The higher V_{bi} of the 3BPIC-*c*F-based device can be attributed to the smaller ΔE_{nr} and larger WF of the ITO/3BPIC-*c*F substrate, resulting in an enlarged V_{OC} [51].

CONCLUSIONS

In summary, we have successfully developed a novel biphosphonic acid molecule with larger dipole moment for SAMs using a central fluorination strategy. Compared to the conventional PEDOT:PSS HEL, the 3BPIC-*c*F exhibits enhanced light transmittance and better interfacial compatibility with the active layer. Due to the larger dipole moment and deeper HOMO energy level of 3BPIC-*c*F, the ITO/3BPIC-*c*F substrate shows a higher WF than the ITO/PEDOT:PSS substrate. The advantages of the 3BPIC-*c*F SAM not only improve hole selectivity but also reduce interfacial impedance and inhibit nonradiative recombination. Consequently, OSCs using 3BPIC-*c*F-based SAMs obtained a champion PCE of 19.34%, much higher than the cells based on PEDOT:PSS (PCE = 18.64%). Moreover, the best PCE of 3BPIC-*c*F-based devices also surpassed that of the 2PACz-based devices (PCE = 18.99%). Notably, the OSCs based on 3BPIC-*c*F also achieved significantly enhanced stability compared to PEDOT:PSS-based devices. Overall, our strategy for central fluorination of biphosphonic acid molecules provides a new choice for designing SAMs materials and paves the way for

further advancements and commercial applications of OSCs.

Received 11 December 2024; accepted 12 February 2025; published online 14 March 2025

1 Zhang G, Zhao J, Chow PCY, *et al.* Nonfullerene acceptor molecules for bulk heterojunction organic solar cells. Chem Rev, 2018, 118: 3447–3507
2 Lin Y, Adilbekova B, Firdaus Y, *et al.* 17% Efficient organic solar cells based on liquid exfoliated WS_2 as a replacement for PEDOT:PSS. Adv Mater, 2019, 31: 1902965
3 Wan X, Li C, Zhang M, *et al.* Acceptor–donor–acceptor type molecules for high performance organic photovoltaics—chemistry and mechanism. Chem Soc Rev, 2020, 49: 2828–2842
4 Li S, Li Z, Wan X, *et al.* Recent progress in flexible organic solar cells. eScience, 2023, 3: 100085
5 Jiang Y, Dong X, Sun L, *et al.* An alcohol-dispersed conducting polymer complex for fully printable organic solar cells with improved stability. Nat Energy, 2022, 7: 352–359
6 Jing J, Dou Y, Chen S, *et al.* Solution sequential deposited organic photovoltaics: from morphology control to large-area modules. eScience, 2023, 3: 100142
7 Li X, Kong X, Sun G, *et al.* Organic small molecule acceptor materials for organic solar cells. eScience, 2023, 3: 100171
8 Zhang G, Lin FR, Qi F, *et al.* Renewed prospects for organic photovoltaics. Chem Rev, 2022, 122: 14180–14274
9 Günther M, Kazerouni N, Blätte D, *et al.* Models and mechanisms of ternary organic solar cells. Nat Rev Mater, 2023, 8: 456–471
10 Lin Y, Wang J, Zhang ZG, *et al.* An electron acceptor challenging fullerenes for efficient polymer solar cells. Adv Mater, 2015, 27: 1170–1174
11 Zhang M, Guo X, Ma W, *et al.* A large-bandgap conjugated polymer for versatile photovoltaic applications with high performance. Adv Mater, 2015, 27: 4655–4660
12 Yuan J, Zhang Y, Zhou L, *et al.* Single-junction organic solar cell with over 15% efficiency using fused-ring acceptor with electron-deficient core. Joule, 2019, 3: 1140–1151
13 Li C, Zhou J, Song J, *et al.* Non-fullerene acceptors with branched side chains and improved molecular packing to exceed 18% efficiency in organic solar cells. Nat Energy, 2021, 6: 605–613
14 Zhu L, Zhang M, Xu J, *et al.* Single-junction organic solar cells with over 19% efficiency enabled by a refined double-fibril network morphology. Nat Mater, 2022, 21: 656–663
15 Chen T, Li S, Li Y, *et al.* Compromising charge generation and recombination of organic photovoltaics with mixed diluent strategy for certified 19.4% efficiency. Adv Mater, 2023, 35: 2300400
16 Duan T, Feng W, Li Y, *et al.* Electronic configuration tuning of centrally extended non-fullerene acceptors enabling organic solar cells with efficiency approaching 19 %. Angew Chem Int Ed, 2023, 62: e202308832
17 Liang H, Bi X, Chen H, *et al.* A rare case of brominated small molecule acceptors for high-efficiency organic solar cells. Nat Commun, 2023, 14: 4707
18 Pang B, Liao C, Xu X, *et al.* Benzo[*d*]thiazole based wide bandgap donor polymers enable 19.54% efficiency organic solar cells along with desirable batch-to-batch reproducibility and general applicability. Adv Mater, 2023, 35: 2300631
19 Yao Z, Cao X, Bi X, *et al.* Complete peripheral fluorination of the small-molecule acceptor in organic solar cells yields efficiency over 19 %. Angew Chem Int Ed, 2023, 62: e202312630
20 Wang C, Chen Q, Zhang C, *et al.* A 6-arm three-blade propeller electron acceptor for organic solar cells with efficiency over 19%. CCS Chem, 2024, 1–11
21 Chen C, Wang L, Xia W, *et al.* Molecular interaction induced dual fibrils towards organic solar cells with certified efficiency over 20%. Nat Commun, 2024, 15: 6865
22 Sun Y, Wang L, Guo C, *et al.* π-extended nonfullerene acceptor for compressed molecular packing in organic solar cells to achieve over 20% efficiency. J Am Chem Soc, 2024, 146: 12011–12019
23 Zheng Z, Hu Q, Zhang S, *et al.* A highly efficient non-fullerene organic solar cell with a fill factor over 0.80 enabled by a fine-tuned hole-transporting layer. Adv Mater, 2018, 30: 1801801
24 Sun W, Wang Y, Zhang Y, *et al.* A cathode interface layer based on 4,5,9,10-pyrene diimide for highly efficient binary organic solar cells. Angew Chem Int Ed, 2022, 61: e202208383
25 Yu Y, Wang J, Chen Z, *et al.* Naphthalene diimide-based cathode interlayer material enables 20.2% efficiency in organic photovoltaic cells. Sci China Chem, 2024, 67: 4194–4201
26 Zeng M, Wang X, Ma R, *et al.* Dopamine semiquinone radical doped PEDOT:PSS: enhanced conductivity, work function and performance in organic solar cells. Adv Energy Mater, 2020, 10: 2000743
27 de Jong MP, van IJzendoorn LJ, de Voigt MJA. Stability of the interface between indium-tin-oxide and poly(3,4-ethylenedioxythiophene)/poly-(styrenesulfonate) in polymer light-emitting diodes. Appl Phys Lett, 2000, 77: 2255–2257
28 Wang Y, Jiang W, Liu SC, *et al.* Durable organic photovoltaics enabled by a morphology-stabilizing hole-selective self-assembled monolayer. Adv Energy Mater, 2023, 14: 2303354
29 Al-Ashouri A, Magomedov A, Roß M, *et al.* Conformal monolayer contacts with lossless interfaces for perovskite single junction and monolithic tandem solar cells. Energy Environ Sci, 2019, 12: 3356–3369
30 Jiang W, Li F, Li M, *et al.* π-expanded carbazoles as hole-selective self-assembled monolayers for high-performance perovskite solar cells. Angew Chem Int Ed, 2022, 61: e202213560
31 Li Z, Sun X, Zheng X, *et al.* Stabilized hole-selective layer for high-performance inverted p-i-n perovskite solar cells. Science, 2023, 382: 284–289
32 Park SM, Wei M, Lempesis N, *et al.* Low-loss contacts on textured substrates for inverted perovskite solar cells. Nature, 2023, 624: 289–294
33 Tan Q, Li Z, Luo G, *et al.* Inverted perovskite solar cells using dimethylacridine-based dopants. Nature, 2023, 620: 545–551
34 Zhang S, Ye F, Wang X, *et al.* Minimizing buried interfacial defects for efficient inverted perovskite solar cells. Science, 2023, 380: 404–409
35 Ullah A, Park KH, Lee YW, *et al.* Versatile hole selective molecules containing a series of heteroatoms as self-assembled monolayers for efficient p-i-n perovskite and organic solar cells. Adv Funct Mater, 2022, 32: 2208793
36 Lin Y, Firdaus Y, Isikgor FH, *et al.* Self-assembled monolayer enables hole transport layer-free organic solar cells with 18% efficiency and improved operational stability. ACS Energy Lett, 2020, 5: 2935–2944
37 Lin Y, Zhang Y, Zhang J, *et al.* 18.9% Efficient organic solar cells based on n-doped bulk-heterojunction and halogen-substituted self-assembled monolayers as hole extracting interlayers. Adv Energy Mater, 2022, 12: 2202503
38 Chen Z, Zhang S, Zhang T, *et al.* Simplified fabrication of high-performance organic solar cells through the design of self-assembling hole-transport molecules. Joule, 2024, 8: 1723–1734
39 Li D, Lian Q, Du T, *et al.* Co-adsorbed self-assembled monolayer enables high-performance perovskite and organic solar cells. Nat Commun, 2024, 15: 7605
40 Truong MA, Funasaki T, Ueberricke L, *et al.* Tripodal triazatruxene derivative as a face-on oriented hole-collecting monolayer for efficient and stable inverted perovskite solar cells. J Am Chem Soc, 2023, 145: 7528–7539
41 Liu H, Xin Y, Suo Z, *et al.* Dipole moments regulation of biphosphonic acid molecules for self-assembled monolayers boosts the efficiency of organic solar cells exceeding 19.7%. J Am Chem Soc, 2024, 146: 14287–14296
42 Deng X, Qi F, Li F, *et al.* Co-assembled monolayers as hole-selective contact for high-performance inverted perovskite solar cells with optimized recombination loss and long-term stability. Angew Chem Int Ed, 2022, 61: e202203088
43 Yip HL, Hau SK, Baek NS, *et al.* Polymer solar cells that use self-assembled-monolayer-modified ZnO/metals as cathodes. Adv Mater, 2008, 20: 2376–2382
44 Kim SY, Cho SJ, Byeon SE, *et al.* Self-assembled monolayers as interface engineering nanomaterials in perovskite solar cells. Adv Energy Mater, 2020, 10: 2002606

45 Liu B, Zhou Q, Li Y, *et al.* Polydentate ligand reinforced chelating to stabilize buried interface toward high-performance perovskite solar cells. Angew Chem Int Ed, 2024, 63: e202317185
46 Afroz MA, Aranda CA, Tailor NK, *et al.* Impedance spectroscopy for metal halide perovskite single crystals: recent advances, challenges, and solutions. ACS Energy Lett, 2021, 6: 3275–3286
47 Proctor CM, Kuik M, Nguyen TQ. Charge carrier recombination in organic solar cells. Prog Polym Sci, 2013, 38: 1941–1960
48 Liu D, Kan B, Ke X, *et al.* Extended conjugation length of nonfullerene acceptors with improved planarity via noncovalent interactions for high-performance organic solar cells. Adv Energy Mater, 2018, 8: 1801618
49 Yu X, Ding P, Yang D, *et al.* Self-assembled molecules with asymmetric backbone for highly stable binary organic solar cells with 19.7 % efficiency. Angew Chem Int Ed, 2024, 63: e202401518
50 Vandewal K, Benduhn J, Nikolis VC. How to determine optical gaps and voltage losses in organic photovoltaic materials. Sustain Energy Fuels, 2018, 2: 538–544
51 Wetzelaer GJAH, Blom PWM. Diffusion-driven currents in organic-semiconductor diodes. NPG Asia Mater, 2014, 6: e110

Acknowledgement This work was supported by the National Key Research and Development Program of China (2019YFA0705900) and the National Natural Science Foundation of China (52273182).

Author contributions Liu H carried out the molecule synthesis, characterization and DFT calculation. Gao X performed the device fabrication and characterization; Zhong H assisted to the material synthesis; Xin Y and Wang R supported the device measurements; Chen Y, Wan X and Kan B provided equipment and experimental support for the project; Liu H and Gao X wrote the original draft of the manuscript; Liu H and Liu Y revised the manuscript. Liu Y directed and supervised the whole project. All authors discussed the results and reviewed the manuscript.

Conflict of interest The authors declare that they have no conflict of interest.

Supplementary information Supplementary materials are available in the online version of the paper.

Hang Liu received his BS degree in 2018 from Xidian University and his MS degree in 2021 from Nankai University. At present, he is a PhD candidate in Prof. Yongsheng Liu's group at Nankai University. His research mainly focuses on solar-energy conversion, including perovskite solar cells and organic solar cells.

Xingbang Gao received his BS degree from China University of Petroleum (East China) in 2016 and his MS degree from Lanzhou University in 2020. He is currently a PhD candidate in Professor Yongsheng Liu's group at Nankai University. His main research interests are perovskite solar cells and perovskite/OPV tandem solar cells.

Yongsheng Liu is a full professor at the College of Chemistry, Nankai University. His research involves organic and organic–inorganic hybrid optoelectronic materials and devices, with specific expertise in perovskite solar cells, organic solar cells, and nanomaterials for applications in energy technology. He has been selected by Clarivate as one of the "Highly Cited Researchers" for seven consecutive years: 2018 through 2024.

双膦酸型自组装单分子层的中心氟化策略实现高效有机太阳能电池

刘航[1†], 高兴邦[1†], 辛雨菲[1], 王若晗[1], 钟浩林[1], 阚斌[3], 万相见[1,2], 陈永胜[1,2], 刘永胜[1,2*]

摘要 目前, 广泛用于正型有机太阳能电池的空穴提取层(HEL)材料是PEDOT:PSS. 然而, PEDOT:PSS的酸性会腐蚀氧化铟锡(ITO)电极, 降低器件的稳定性. 本文采用中心氟化策略, 设计合成了一种双膦酸型自组装单分子层(SAM)材料 3BPIC-*c*F. 与PEDOT:PSS相比, 3BPIC-*c*F修饰的ITO基底具有更高的光透过率和更好的界面相容性. 氟原子的引入使得3BPIC-*c*F具有更大的偶极矩和更深的最高占据轨道能级, 导致ITO/3BPIC-*c*F基底具有比ITO/PEDOT:PSS基底更大的功函数. 这些优势有利于空穴的提取, 降低界面阻抗并抑制界面处的非辐射复合. 使用3BPIC-*c*F作为HEL的有机太阳能电池实现了19.34%的光伏效率, 优于PEDOT:PSS器件(PCE = 18.64%). 此外, 基于3BPIC-*c*F的光伏器件具有比基于PEDOT:PSS的器件更高的稳定性. 本研究为面向高效有机太阳能电池中SAM分子的设计与合成提供了有价值的指导.

